INSTITUTE OF PHYSICS PUBLISHING SMART MATERIALS AND STRUCTURES
Smart Mater. Struct. **14** (2005) 1163–1171 doi:10.1088/0964-1726/14/6/009

Numerical simulation and analysis of an electroactuated beam using a radial basis function

Y Liu[1], K M Liew[2], Y C Hon[3,4] and X Zhang[1]

[1] Department of Engineering Mechanics, Tsinghua University, Beijing 100084, People's Republic of China
[2] Center for Advanced Numerical Engineering Simulations, School of Mechanical and Production Engineering, Nanyang Technological University, Nanyang Avenue, Singapore 639798, Singapore
[3] Department of Mathematics, City University of Hong Kong, 83 Tat Chee Avenue, Kowloon, Hong Kong

E-mail: maychon@cityu.edu.hk

Received 10 September 2004, in final form 6 July 2005
Published 20 September 2005
Online at stacks.iop.org/SMS/14/1163

Abstract
In this paper an analysis of microelectromechanical systems (MEMS) is performed by using the recently developed radial basis function (RBF) collocation method. Formulations for both static and dynamic analyses of electroactuated beams are derived. The spatial variables in the formulated model are approximated by the RBF whilst the central difference scheme and Newmark scheme are adopted to integrate the ordinary differential equations with respect to time. The Newton–Raphson scheme is also utilized to solve effectively the system of nonlinear equations resulting from the electric force. Numerical validations show that, with only a few nodes used in the computation, the RBF collocation method gives an identical result to other numerical methods, such as the reproducing kernel particle method, and experiments. The effects of residual stress and initial gap length on the pull-in voltage are also investigated.

1. Introduction

The last decade of the 20th century witnessed the rapid development of microelectromechanical systems (MEMS). Advanced technologies for fabricating a variety of MEMS devices have developed to meet the high demand from industries. On the other hand, there is still a need for computational tools that can allow engineers to quickly design and optimize these micromachines [1]. Much effort has been devoted to seeking simple and efficient simulation methods with high accuracy.

Modeling schemes for MEMS components can be roughly categorized into two groups. The first group can be called reduced-order models (macromodels or lumped models) which highlight the major behavior and influential factors of the MEMS component by using only very few degrees of freedom (typically one or two). This allows the designers to simulate the MEMS components quickly. For instance, Legtenberg *et al* [2] theoretically analyzed an electrostatic actuator consisting of a laterally compliant cantilever beam and a fixed curved electrode by using energy methods. Huang *et al* [3] developed a static electromechanical model to predict the effective stiffness constant and the critical collapse voltage for several typical bridge geometries in a capacitive micromachined switch. They also proposed a nonlinear dynamic model for analyzing the switching speed and the Q-factor. Pamidighantam *et al* [4] derived a closed-form expression for the pull-in voltage of fixed–fixed beams and fixed–free beams from the known expression for a simple lumped spring–mass system. Bochobza-Degani and Nemirovsky [5] proposed a pull-in model with two degrees of freedom to predict the pull-in parameters of electrostatic actuators. Younis *et al* [6] obtained a macromodel for microbeam-based MEMS by discretizing the distributed-

[4] Author to whom any correspondence should be addressed.

parameter system, using a Galerkin procedure, into a finite degree of freedom system consisting of ordinary differential equations (ODEs) for the time variable. Cheng *et al* [7] utilized a capacitance-based generalized model to predict the static behaviors of rigid and deformable electrostatic actuator systems. They derived an expression for the capacitance under various electrode configurations.

The performance of these reduced-order models, however, relies heavily on the choice of degrees of freedom. The rationality of these models is often examined by the second group of MEMS modeling schemes—solving partial differential equations (PDEs) corresponding to the physical fields in the MEMS component. This then involves the traditional computational methods such as the finite element method (FEM), boundary element method (BEM), finite difference method (FDM) and finite volume method (FVM). Although some common commercial software systems, such as ABAQUS, ANSYS, FASTCAP, can be employed in the simulation of MEMS components, many researchers and engineers still see the need for improved numerical methods for simulating MEMS models. In this respect, Aluru and White [8] developed an efficient algorithm for self-consistent analysis of three-dimensional MEMS in which a multilevel Newton technique has been employed to solve the coupled electromechanical system. The method can utilize a black-box FEM solver for mechanical analysis and a black-box BEM solver for electrostatic analysis. On the basis of a sequential field-coupling approach, Collenz *et al* [9] recently proposed a new FEM method in which the traditional way of correcting the applied load during the process of deformation is replaced by applying electrostatic loads incrementally. This method is more effective for handling the MEMS simulation case with large displacements.

Although the finite difference and finite element methods have been widely used in engineering and industrial applications over the last few decades, one of the major disadvantages of these traditional methods is their dependence on computational grids or meshes. In fact, the meshing can occupy 60–70% of the time in a finite element analyzing process. This hinders their application to high dimensional or geometrically complex problems. The rapid development of meshless methods in the last decade has overcome this mesh-dependent disadvantage. Different kinds of meshless methods [10–15] have been proposed and shown to have advantages over the traditional methods especially in problems of extremely large deformation, fracture, impact and explosion. Meshless methods have also shown great potential in the fields of computational fluid dynamics (CFD), thermal analysis and magnetic problems. See [16, 17] and references therein for an overview of the meshless methods.

Aluru [18] first applied the meshless reproducing kernel particle method (RKPM) in the analysis of electroactuated beams and pressure sensors. He and his co-workers also proposed a volume-type meshless method called the finite cloud method (FCM) and a boundary-type meshless method called the boundary cloud method (BCM). Li and Aluru [19] compared the computed static pull-in voltages of microbeams with and without the consideration of large deformation. Ohs and Aluru [20] employed the FCM in the numerical analysis of coupled electromechanical fields in piezoelectric structures

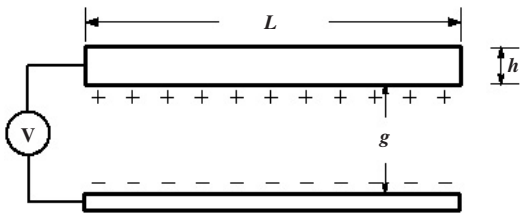

Figure 1. Schematic illustration of the electroactuated beam.

with both relaxation and fully coupled schemes. Recently, Li and Aluru combined the FCM and BCM for an efficient mixed-domain analysis of electrostatic MEMS [21], in which the FCM was employed to solve for the mechanical deformation field and the BCM was used to analyze the exterior electrostatic domain.

In the last decade, the development in applying the radial basis functions (RBFs) as a truly meshless method for approximating the solutions of PDEs has drawn the attention of many researchers and engineers. One of these domain-type meshless methods developed by Kansa in 1990 [10] is obtained simply by directly collocating the RBFs, particularly the multiquadric (MQ) basis, for the numerical approximation of the solution. Its nice properties including truly meshless, space-dimension-independent and special convergence orders has been proved for some RBF functions [22]. Hon *et al* recently extended the RBF method to solve various ordinary and partial differential equations including the biphasic and triphasic mixture model for tissue engineering problems [23, 24] and the simulation of three-dimensional tidal flows in coastal waters with a multilayer model [25].

In this paper, the RBF collocation method is further extended to analyze an important aspect of a MEMS—its electroactuated structures for thin beams with high length–thickness ratio. In section 2, the governing equation and boundary conditions of the beam model are briefly reviewed and nondimensionalized. The approximation scheme of the RBF method is investigated and the discretized equations are derived in section 3. Numerical validations including static and dynamic examples are given in section 4. The work is concluded in section 5.

2. Governing equation

As shown in figure 1, the motion of an electroactuated beam can be described by the following governing equation:

$$\rho\frac{\partial^2 u}{\partial t^2}+\tilde{E}I\frac{\partial^4 u}{\partial x^4}-T_b\frac{\partial^2 u}{\partial x^2}=\frac{w\varepsilon_0 V^2}{2g^2}\left(1+0.65\frac{g}{w}\right), \quad (1)$$

where $u(x,t)$ denotes the deflection of the beam, x and t are spatial and time variables, respectively, $T_b=\hat{\sigma}wh$ is the axial force induced by the residual stress σ_0, where the effective residual stress $\hat{\sigma}=\sigma_0(1-\nu)$, w is the width of the beam and h is the thickness. ρ, $\tilde{E}$, ν and $I=\frac{wh^3}{12}$ represent the density per unit length, the effective Young's modulus, the Poisson ratio and the inertia moment, respectively. For $w>5h$ (plane strain case), $\tilde{E}=\frac{E}{1-\nu^2}$; for $w\approx h$ (plane stress case), $\tilde{E}$

is the Young's modulus E. The right-hand-side (RHS) term represents the electric force, where $\varepsilon_0 = 8.8542$ F m^{-1} is the permittivity of free space, V is the applied voltage difference between the beam and the ground electrode, $g = g_0 - u$ is the gap between the beam and the electrode and g_0 is the initial gap length. The second RHS term is due to a correction of the fringe effect.

When a driving voltage is applied, the beam will be deflected by the pressure induced by the electrostatic field. As the shape of the beam varies, the charge is redistributed along the beam, which causes the beam to deflect further. Note that the RHS terms in equation (1) result in high nonlinearity when the beam approaches the electrode. If the applied voltage exceeds a critical value, the beam will collapse to the ground electrode. This critical value, called the pull-in voltage, is of great importance in the modeling of electroactuated structures.

Typical boundary conditions for the beam equation include clamped end, simply supported end, free end. The clamped boundary condition

$$\begin{aligned} u &= 0, \\ \theta &= \frac{\partial u}{\partial x} = 0, \end{aligned} \tag{2}$$

and the free boundary condition

$$\begin{aligned} M &= -EI\frac{\partial^2 u}{\partial x^2} = 0, \\ Q &= -EI\frac{\partial^3 u}{\partial x^3} = 0, \end{aligned} \tag{3}$$

are frequently encountered in the analysis of MEMS components, where θ, M, Q denote the slope angle, the bending moment and the shear force, respectively.

The initial conditions are

$$\begin{aligned} u(x,0) &= u_0(x), \\ \frac{\partial u(x,0)}{\partial t} &= v_0(x). \end{aligned} \tag{4}$$

As mentioned before, the typical scale of the MEMS component is of the order of microns. In order to avoid unnecessary error produced by operations on variables whose orders of magnitude are greatly different, we introduce the following dimensionless variables:

$$\begin{aligned} &\bar{u} = \frac{u}{L}, \qquad \bar{x} = \frac{x}{L}, \qquad \bar{t} = \frac{t}{T}, \\ &\bar{w} = \frac{w}{L}, \qquad \bar{h} = \frac{h}{L}, \qquad \bar{g} = \frac{g}{L}, \\ &\bar{g}_0 = \frac{g_0}{L}, \qquad \bar{T}_b = \frac{T_b L^2}{\tilde{E} I}, \end{aligned} \tag{5}$$

where the characteristic time is defined as $T = \sqrt{\frac{\rho L^4}{\tilde{E} I}}$. Substituting the above dimensionless variables into equation (1), the dimensionless beam equation becomes

$$\frac{\partial^2 \bar{u}}{\partial \bar{t}^2} + \frac{\partial^4 \bar{u}}{\partial \bar{x}^4} - \bar{T}_b \frac{\partial^2 \bar{u}}{\partial \bar{x}^2} = A_1 \bar{g}^{-2} + A_2 \bar{g}^{-1}, \tag{6}$$

with the dimensionless coefficients

$$A_1 = \frac{w\varepsilon_0 V^2 L}{2\tilde{E} I}, \qquad A_2 = \frac{0.65 A_1}{\bar{w}}. \tag{7}$$

The corresponding dimensionless boundary conditions are

$$\bar{u} = 0, \qquad \frac{\partial \bar{u}}{\partial \bar{x}} = \theta = 0, \qquad \text{for clamped end,} \tag{8}$$

$$\frac{\partial^2 \bar{u}}{\partial \bar{x}^2} = -\frac{ML}{\tilde{E} L} = 0, \qquad \frac{\partial^3 \bar{u}}{\partial \bar{x}^3} = -\frac{QL^2}{\tilde{E} I} = 0, \quad \text{for free end.} \tag{9}$$

The initial conditions can also be nondimensionlized as

$$\bar{u}(\bar{x}, \bar{t}) = \frac{u_0}{L}, \tag{10}$$

$$\frac{\partial \bar{u}(\bar{x}, \bar{t})}{\partial \bar{t}} = \frac{v_0 T}{L}. \tag{11}$$

3. RBF approximation and discretization

The dimensionless governing equation and boundary conditions given in section 2 will be discretized by using the proposed RBF collocation method in this section. For verification purposes, the following RBF basis functions are adopted:

$$\text{Multiquadric (MQ) basis:} \qquad \Phi_I(\bar{x}) = \sqrt{\|\bar{x} - \bar{x}_I\|^2 + c^2}, \tag{12}$$

$$\text{Power spline basis:} \qquad \Phi_I(\bar{x}) = \|\bar{x} - \bar{x}_I\|^n, \tag{13}$$

where $\bar{x}_I$ is the coordinate of node I and $c > 0$ is called the shape parameter whose value influences the accuracy of the MQ basis function. The MQ function varies from a cone-like interpolated surface to a bowl-like surface, as the value of c increases. The MQ basis was rated one of the best among 29 scattered data interpolation schemes based on tests on accuracy, stability, efficiency, memory requirement and ease of implementation by Franke [26]. The choice of the shape parameter c will be discussed through numerical experiments. For the power spline basis function r^n, there is no need to choose a shape parameter, and its accuracy depends on the degree $n = 2k - 1, k \in \mathrm{N}^+$. Since the highest derivative order is four in the beam equation, we examine only r^5 and r^7 in the numerical examples. The derivatives of the basis function can easily be obtained from the chain rule:

$$\frac{\mathrm{d}\Phi_I(\bar{x})}{\mathrm{d}\bar{x}} = \frac{\mathrm{d}\Phi_I(\bar{x})}{\mathrm{d}r}\frac{\mathrm{d}r}{\mathrm{d}\bar{x}}, \tag{14}$$

where $r = \|\bar{x} - \bar{x}_I\|$. The higher order derivatives can be derived in a similar way.

At each evaluation point $\bar{x}$, the RBF collocation method approximates the solution by the following linear combination of basis functions:

$$\bar{u}(\bar{x}, \bar{t}) \approx u^h(\bar{x}, \bar{t}) = \sum_{I=1}^{N} \Phi_I(\bar{x}) u_I(\bar{t}) = \mathbf{\Phi}^{\mathrm{T}}(\bar{x})\mathbf{U}(\bar{t}), \tag{15}$$

where u_I is the nodal parameter and N is the total number of nodes. It is noted here that, unlike in the FEM, the nodal parameter is not the nodal value of the corresponding variable.

Substituting equation (15) into the governing equation (6) gives the following matrix equation:

$$\mathbf{M}\ddot{\mathbf{U}} + (\mathbf{K} - \mathbf{K}^{\sigma})\mathbf{U} = \mathbf{F}^{\mathrm{elec}}, \tag{16}$$

where

$$\begin{aligned} M_{IJ} &= \Phi_J(\bar{x}_I), \\ K_{IJ} &= \frac{\mathrm{d}^4\Phi_J(\bar{x}_I)}{\mathrm{d}\bar{x}^4}, \\ K^{\sigma}_{IJ} &= \bar{T}_b\frac{\mathrm{d}^2\Phi_J(\bar{x}_I)}{\mathrm{d}\bar{x}^2}, \\ F^{\mathrm{elec}}_I &= A_1[\bar{g}(\mathbf{U})]^{-2} + A_2[\bar{g}(\mathbf{U})]^{-1}. \end{aligned} \tag{17}$$

The second-order ODE equation (16) can be solved directly by many integration methods. In this paper, the central difference and the Newmark methods are employed. For the central difference method, the derivative of second order with respect to time is approximated by

$$\ddot{\mathbf{U}} = \frac{\mathbf{U}^{n+1} - 2\mathbf{U}^n + \mathbf{U}^{n-1}}{\Delta\bar{t}^2}, \tag{18}$$

where the superscript n refers to the nodal parameter at the nth step with dimensionless time step size $\Delta\bar{t} = \frac{\Delta t}{T}$. Substituting the above equation into equation (16) yields the following explicit discretized equation for iteratively computing the approximation $\mathbf{U}^{n+1}$:

$$\frac{\mathbf{M}}{\Delta\bar{t}^2}\mathbf{U}^{n+1} = (\mathbf{F}^{\mathrm{elec}})^n - \left(\mathbf{K} - \mathbf{K}^{\sigma} - \frac{2\mathbf{M}}{\Delta\bar{t}^2}\right)\mathbf{U}^n - \frac{\mathbf{M}}{\Delta\bar{t}^2}\mathbf{U}^{n-1}. \tag{19}$$

The Newmark method approximates the nodal parameters and their derivatives with respect to time as

$$\begin{aligned} \dot{\mathbf{U}}^{n+1} &= \dot{\mathbf{U}}^n + [(1-\delta)\ddot{\mathbf{U}}^n + \delta\ddot{\mathbf{U}}^{n+1}]\Delta\bar{t} \\ \mathbf{U}^{n+1} &= \mathbf{U}^n + \dot{\mathbf{U}}^n\Delta\bar{t} + [(\tfrac{1}{2} - \alpha)\ddot{\mathbf{U}}^n + \alpha\ddot{\mathbf{U}}^{n+1}]\Delta\bar{t}^2, \end{aligned} \tag{20}$$

where the parameters $\delta = 0.5$ and $\alpha = 0.25$ are adopted. Substituting the above two equations into equation (16), the formulation of the Newmark scheme can be written as

$$\begin{aligned} &\left(\mathbf{K} - \mathbf{K}^{\sigma} + \frac{\mathbf{M}}{\alpha\Delta\bar{t}^2}\right)\mathbf{U}^{n+1} - (\mathbf{F}^{\mathrm{elec}})^{n+1} \\ &= \mathbf{M}\left[\frac{\mathbf{U}^n}{\alpha\Delta\bar{t}^2} + \frac{\dot{\mathbf{U}}^n}{\alpha\Delta\bar{t}} + \left(\frac{1}{2\alpha} - 1\right)\ddot{\mathbf{U}}^n\right]. \end{aligned} \tag{21}$$

Note that the electric force term $(\mathbf{F}^{\mathrm{elec}})^{n+1} \equiv \mathbf{F}^{\mathrm{elec}}(\mathbf{U}^{n+1})$ is a nonlinear function of the nodal parameters at each $(n+1)$th time step. In order to solve this nonlinear equation (21), we employ the following Newton–Raphson method:

$$\begin{aligned} &\left(\mathbf{K} - \mathbf{K}^{\sigma} + \frac{\mathbf{M}}{\alpha\Delta\bar{t}^2} - \frac{\partial\mathbf{F}^{\mathrm{elec}}}{\partial\mathbf{U}}\right)\Delta\mathbf{U}^{n+1,m+1} \\ &= (\mathbf{F}^{\mathrm{elec}})^{n+1,m} + \mathbf{M}\left[\frac{\mathbf{U}^n}{\alpha\Delta\bar{t}^2} + \frac{\dot{\mathbf{U}}^n}{\alpha\Delta\bar{t}} + \left(\frac{1}{2\alpha} - 1\right)\ddot{\mathbf{U}}^n\right] \\ &\quad + \left(\mathbf{K} - \mathbf{K}^{\sigma} + \frac{\mathbf{M}}{\alpha\Delta\bar{t}^2}\right)\mathbf{U}^{n+1,m}, \end{aligned} \tag{22}$$

where the superscript m denotes the values of the nodal parameters at the mth iteration step. At the next $(m+1)$th iteration step, we have $\mathbf{U}^{n+1,m+1} = \mathbf{U}^{n+1,m} + \Delta\mathbf{U}^{n+1,m+1}$.

The iteration will be terminated by using the following criterion:

$$\frac{\sqrt{(\mathbf{u}^{n+1,m+1} - \mathbf{u}^{n+1,m})^{\mathrm{T}}(\mathbf{u}^{n+1,m+1} - \mathbf{u}^{n+1,m})}}{\sqrt{(\mathbf{u}^{n+1,m+1})^{\mathrm{T}}(\mathbf{u}^{n+1,m+1})}} < \varepsilon, \tag{23}$$

where $\mathbf{u}$ is the vector containing the deflections of evaluation points and ε is a user-defined error tolerance, which is set as 10^{-4} in this paper.

For clamped end boundary condition, the discretized equations are

$$\mathbf{\Phi}^{\mathrm{T}}(\bar{x}_e)\mathbf{U}^{n+1} = 0, \tag{24}$$

$$\left(\frac{\partial\mathbf{\Phi}(\bar{x}_e)}{\partial\bar{x}}\right)^{\mathrm{T}}\mathbf{U}^{n+1} = 0, \tag{25}$$

and, for free end boundary conditions,

$$\left(\frac{\partial^2\mathbf{\Phi}(\bar{x}_e)}{\partial\bar{x}^2}\right)^{\mathrm{T}}\mathbf{U}^{n+1} = 0, \tag{26}$$

$$\left(\frac{\partial^3\mathbf{\Phi}(\bar{x}_e)}{\partial\bar{x}^3}\right)^{\mathrm{T}}\mathbf{U}^{n+1} = 0, \tag{27}$$

where $\bar{x}_e$ denotes the end points of the beam, which equals 0 or 1 in the above dimensionless beam equation.

The static analysis also plays an important role in the numerical solution for the MEMS component. For the static case, the first term of the discretized governing equation (16) vanishes. This gives the following nonlinear equation:

$$(\mathbf{K} - \mathbf{K}^{\sigma})\mathbf{U} = \mathbf{F}^{\mathrm{elec}}, \tag{28}$$

which can also be solved by the Newton–Raphson iterative method as follows:

$$\left[\mathbf{K} - \mathbf{K}^{\sigma} - \left(\frac{\partial\mathbf{F}^{\mathrm{elec}}}{\partial\mathbf{U}}\right)^m\right]\Delta\mathbf{U}^{m+1} = (\mathbf{F}^{\mathrm{elec}})^m - (\mathbf{K} - \mathbf{K}^{\sigma})\mathbf{U}^m, \tag{29}$$

using a similar criterion of convergence:

$$\frac{\sqrt{(\mathbf{u}^{m+1} - \mathbf{u}^m)^{\mathrm{T}}(\mathbf{u}^{m+1} - \mathbf{u}^m)}}{\sqrt{(\mathbf{u}^{m+1})^{\mathrm{T}}(\mathbf{u}^{m+1})}} < \varepsilon. \tag{30}$$

We remark here that the boundary conditions can be collocated similarly using the dynamic analysis equations (24) and (26) with the only difference being that the superscript $n+1$ is dropped.

4. Numerical examples

If the total numbers of nodes and evaluation points are the same, the system will become overdetermined since each boundary point gives two independent equations. The overdetermined system can be solved in a least-squares way [12]. In this paper a new strategy of introducing more nodes will be adopted. This is based on the flexibility of the proposed RBF method: the total numbers of centers and evaluation points need not be the same. Suppose that there are N_i inner evaluation points and two boundary evaluation points, which require $N_i + 4$ nodes to determine the solution uniquely. The first $N_i + 2$ nodes are distributed identically with the evaluation points and numbered sequentially along the beam. The $(N_i + 3)$th node lies at the location $2x_1 - x_2$ and the last node lies at $2x_{N_i+2} - x_{N_i+1}$.

In the following examples, we take $N_i = 19$. Two strategies for distributing the collocation points (nodes) are adopted: one is distributing them along the beam uniformly and the other is using the Chebyshev–Gauss–Lobatto (Chebyshev for short) distribution defined as

$$\bar{x}_i = \frac{1}{2}\left(1 - \cos\frac{i-1}{N_i+1}\pi\right). \tag{31}$$

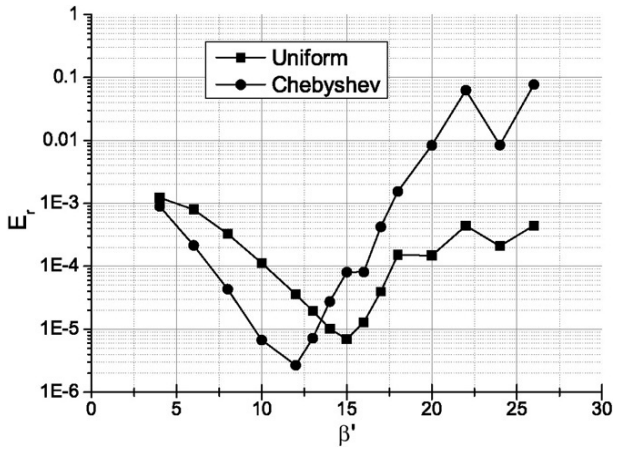

Figure 2. The variation of the relative error E_r with respect to the parameter β'; clamped–clamped beam.

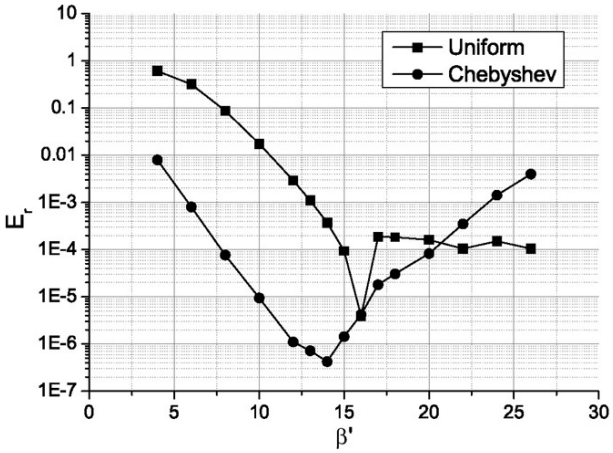

Figure 3. The variation of the relative error E_r with respect to the parameter β'; cantilevered beam.

4.1. Choice for the optimal parameter

The value of the shape parameter c is vital to the accuracy of the MQ basis. Hon *et al* [23] showed that if the value of β lies in the range from 8 to 20, the RBF gave a good approximation to the solution for a biphasic mixture model of charged and hydrated soft tissues, where $c = \beta d_{\min}$ and $d_{\min}$ is the minimum distance between any two collocation points. Wong *et al* [25] adopted the value of $\beta = 0.815$ when solving a multilayer model for a coastal system with MQ functions and a multizone domain decomposition technique. Zhang *et al* [22] has recently shown that the value of $c = 6$ can yield high accuracy for analyzing a 2D elastostatic problem in a rectangular domain. Wang and Liu [27] numerically obtained the optimal parameters $c = 1.42$ and $q = 1.03$ for the general MQ basis $\Phi_I(x) = (\|x - x_I\|^2 + c^2)^q$ used in their radial point interpolation meshless method.

In this section, the optimal range of c is investigated via examples where beams are only subject to uniformly distributed loading q. The parameter c is defined as $\beta' d_{\text{ave}}$, where d_{ave} is the average of the distances between any two adjacent collocation points. The analytical expressions for the deflection are

$$u = \frac{q}{24EI}(x^4 - 2x^3L + x^2L^2), \quad \text{for clamped–clamped case}$$
$$u = \frac{q}{24EI}(x^4 - 4x^3L + 6x^2L^2), \quad \text{for cantilever case.} \tag{32}$$

The relative error is defined as

$$E_r = \frac{\sqrt{(\mathbf{u}^{\text{num}} - \mathbf{u}^{\text{e}})^{\text{T}}(\mathbf{u}^{\text{num}} - \mathbf{u}^{\text{e}})}}{\sqrt{(\mathbf{u}^{\text{e}})^{\text{T}}(\mathbf{u}^{\text{e}})}} \tag{33}$$

and the superscripts num and e denote numerical results and analytical results, respectively.

Figure 2 shows the relative error with the variation of β' of the clamped–clamped beam. In this case, the uniform distribution gives higher accuracy when $\beta' = 14$–26, while the Chebyshev distribution behaves better when $\beta' = 4$–13. Both the distributions yield acceptable results when $\beta' = 4$–18. The variation of E_r for the cantilevered beam is plotted in figure 3. The accuracy of the Chebyshev distribution is higher than the uniform one in most ranges, especially remarkably when $\beta' < 14$. $\beta' = 6$–23 for the Chebyshev distribution and $\beta' = 13$–26 for the uniform distribution are acceptable ranges.

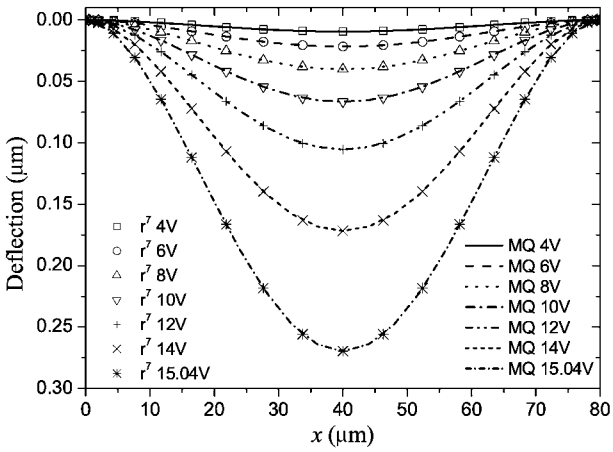

Figure 4. Deflection curve of a clamped–clamped beam.

The accuracy of r^7 and r^5 bases for these two examples are also investigated. For the clamped–clamped case, the relative errors of the r^7 basis are 3.95×10^{-4} for the uniform distribution and 3.75×10^{-5} for the Chebyshev distribution and those of the r^5 basis are about one order larger than those for the r^7 basis. For the cantilevered case, both the results (for the r^7 and r^5 bases) are not accurate enough.

4.2. Electroactuated clamped–clamped beam

The dimension of the beam is 80 μm (length) $\times$ 10 μm (width) $\times$ 0.5 μm (thickness). The initial gap length $g_0 = 0.7$ μm. The effective Young's modulus $\tilde{E} = 169$ GPa and the density per unit volume is 2231 kg m^{-3}. Both static and dynamic analysis are carried out in this example.

The static deflection curves are displayed in figure 4, where the applied voltages vary from 4 to 15.04 V, and the

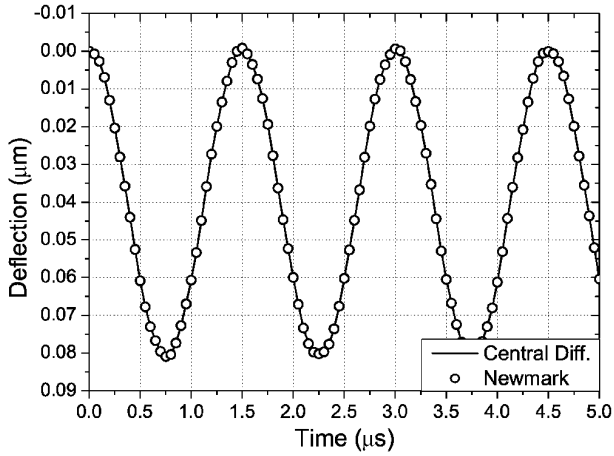

Figure 5. Deflection of the mid-point of a clamped–clamped beam with respect to time. Applied voltage: 8 V. (The label 'Central Diff.' represents the central difference scheme.)

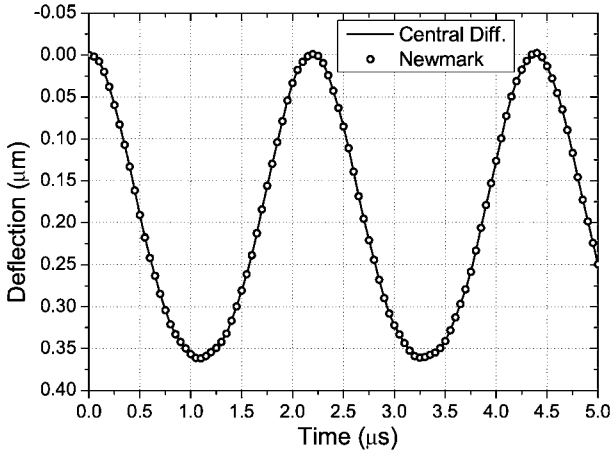

Figure 7. Deflection of the mid-point of a clamped–clamped beam with respect to time. Applied voltage: 13.6 V.

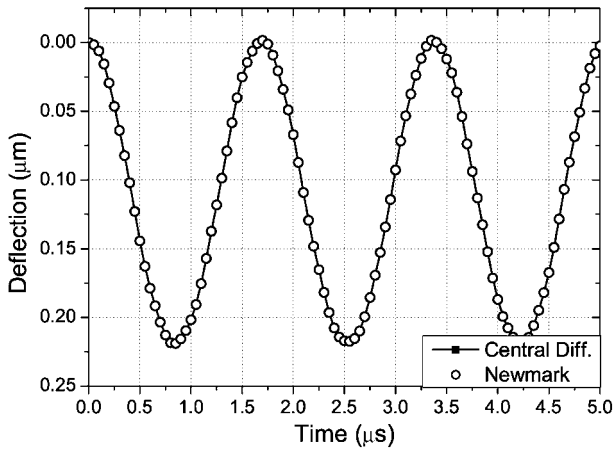

Figure 6. Deflection of the mid-point of a clamped–clamped beam with respect to time. Applied voltage: 12 V.

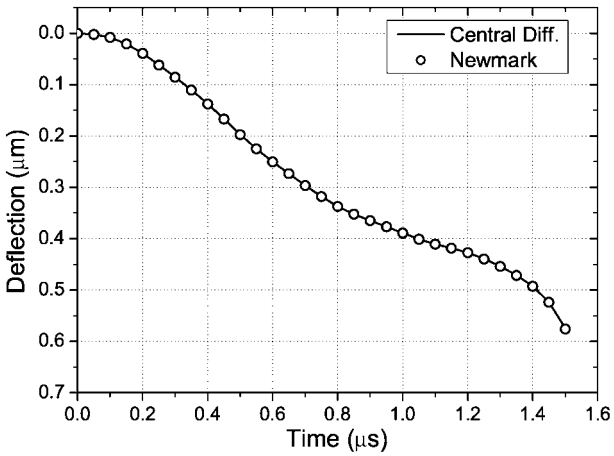

Figure 8. Deflection curve of the mid-point of a clamped–clamped beam with respect to time under the pull-in voltage.

r^7 basis with the Chebyshev distribution and the MQ basis with the uniform distribution and the parameter $\beta' = 13$ are employed in the computation. The results from the two methods are nearly undistinguishable, and they agree well with those from the RKPM [18]. As is shown, the nonlinearity caused by the electric force increases rapidly on approaching pull-in status. The calculated static pull-in voltages of the r^7 and MQ bases are 15.05 and 15.06 V, respectively. The relative errors are below 1% compared to the experimental result of 15.17 V reported in [28]. Our results are closer to that from the RKPM [18] which is 15.08 V. It is remarked here that only a very small number of nodes (23 nodes compared with 100 nodes in the RKPM) are used in the computation. The proposed RBF method also does not need to compute the multiple Gauss integration required in the RKPM computation. This advantage is particularly attractive for handling problems in higher dimensional cases.

In dynamic analysis, the central difference and Newmark schemes with the r^7 basis and uniform distribution are adopted. The sizes of the time step are 1 ns for the central difference scheme and 5 ns for the Newmark scheme. Figures 5–7 display the deflection curves with respect to time at the mid-point of the beam under voltages of 8, 12 and 13.6 V. The dynamic pull-in voltage is 13.8 V. Both the deflection curves and the pull-in voltage coincide excellently with those from the RKPM (the dynamic pull-in voltages reported in [18] and [28] are 13.7 V). The deflection curve under the pull-in voltage is also displayed in figure 8.

It is well known that the central difference scheme is conditionally stable. The classical FEM analysis has concluded that the critical time step size Δt_{cr} has a relationship with the minimum element size. The critical time step size of the RBF collocation method is also investigated and it is found that $\Delta \bar{t}_{\mathrm{cr}}$ is about 2.7 ns for the uniform distribution and 0.30 ns for the Chebyshev distribution. It is not surprising that the Chebyshev distribution has a smaller $\Delta \bar{t}_{\mathrm{cr}}$ since its minimum nodal distance is about a quarter in the uniform distribution. As the Newmark scheme is unconditionally stable with the parameters chosen in this paper, it is recommended that the Newmark scheme should be adopted when Chebyshev nodes are used.

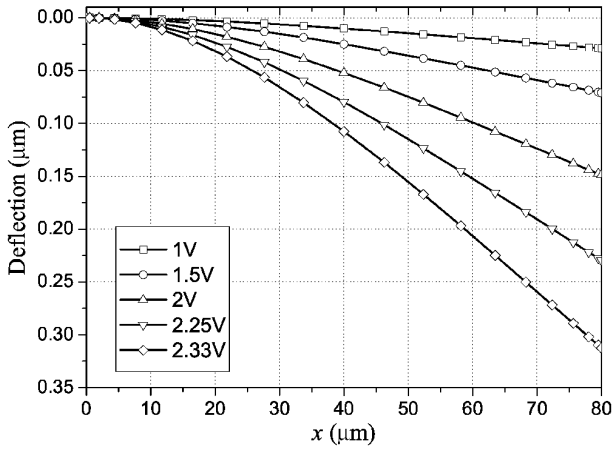

Figure 9. Deflection curve of a cantilevered beam.

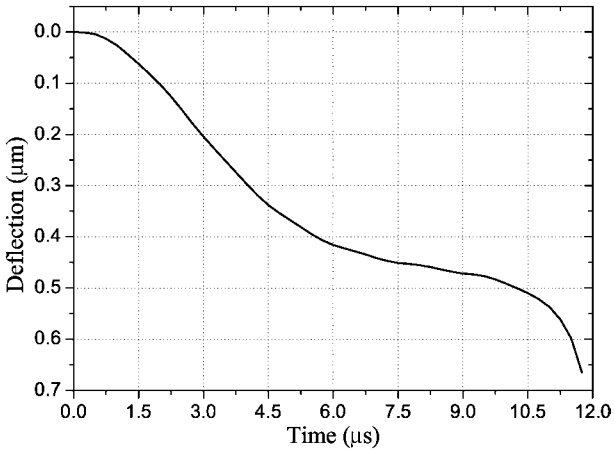

Figure 11. Deflection of the free end of a cantilevered beam with respect to time under the pull-in voltage.

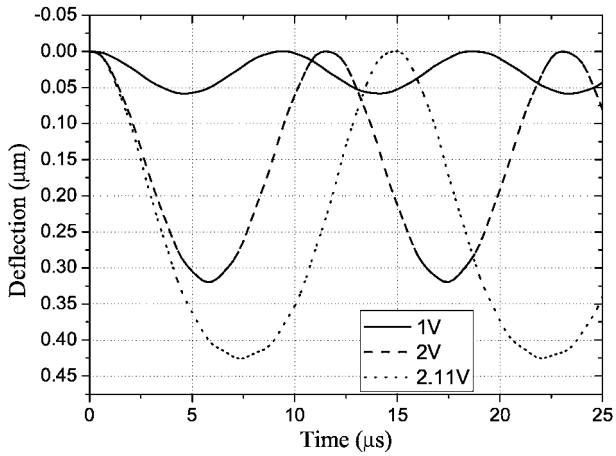

Figure 10. Deflection of the free end of a cantilevered beam with respect to time. Applied voltage: 1, 2 and 2.11 V.

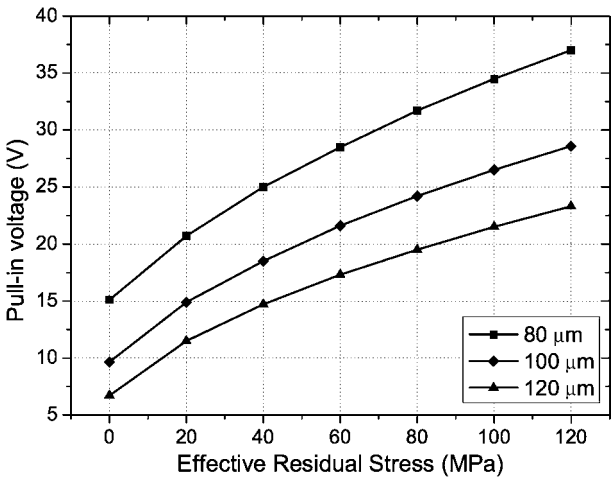

Figure 12. Influence of residual stress on the pull-in voltage.

4.3. Electroactuated cantilevered beam

The geometric and physical parameters adopted in the following electroactuated example are the same as those given in the previous example. In the computation the MQ basis with the Chebyshev distribution is adopted in this example. Figure 9 shows the static deflection of the beam under different driving voltages of 1–2.33 V. The computed static pull-in voltage is 2.34 V, which matches the result given by Aluru [18].

The variations of the deflection at the free end with respect to time under different voltages 1, 2 and 2.11 V are shown in figure 10. The Newmark integration scheme with a time step $\Delta t = 5$ ns and parameter $\beta' = 6$ in the MQ basis are used. Figure 11 shows the deflection curve at the free end with respect to the pull-in voltage 2.12 V, which is again in good agreement with the result from the RKPM given in [18].

4.4. Influences of initial gap length and residual stress

The computational results for a clamped–clamped beam under residual stress is compared with the experimental data. The width and the thickness of the beam are 100 and 1.5 μm respectively. The effective Young's modulus is 166 GPa; the residual axial load is $T_b = 0.0009$ N; and the initial gap is 1.18 μm. The length of the beam varies from 210 to 510 μm. Table 1 gives the comparison between the experimental data [29] and computational results obtained by using the r^7 basis and uniform distribution. It can be observed from table 1 that the two results agree well. The largest deviation occurs when the length of the beam is $L = 510$ μm (the longest in the example) with a relative difference of 4.26% which may be caused by the influence of large deformation.

Table 1. Comparison of static pull-in voltages between experimental and numerical results for different beam lengths.

Length (μm)	Experimental results (V) [29]	RBF results (V)	Relative error (%)
210	27.95	27.40	1.97
310	13.78	13.79	0.07
410	9.13	8.75	4.16
510	6.57	6.29	4.26

The influences of gap length and residual stress on the static pull-in voltage are also investigated. Figure 12 shows the variation of the pull-in voltage for a clamped–clamped

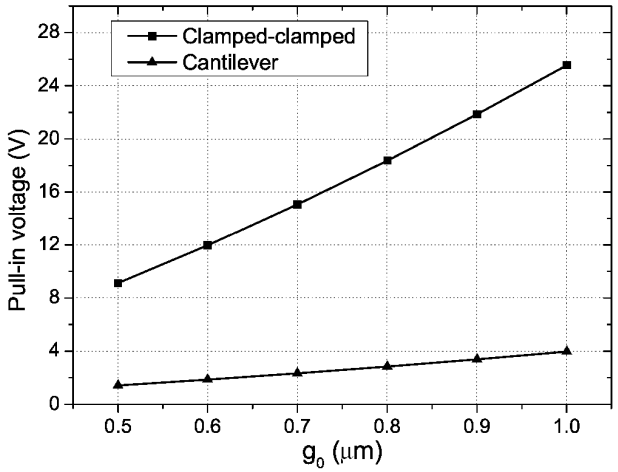

Figure 13. Influence of initial gap length on the pull-in voltage.

beam with the geometric and physical parameters listed in section 4.2, except that the effective residual stress varies from 0 to 120 MPa. The results are obtained by using the r^7 basis and uniform distribution. As shown in figure 12, the static pull-in voltage increases as the residual stress increases, whilst the magnitude of the increase decreases if the residual stress gets higher.

The influence of the initial gap length is shown in figure 13. The parameters are again the same as in section 4.2. In the computation, initial gap lengths from 0.5 to 1.0 μm are considered. The clamped–clamped beam is analyzed by using the r^7 basis and the uniform distribution and the cantilevered beam is analyzed by using the MQ basis with parameter $\beta' = 13$ and the Chebyshev distribution. In both cases, the static pull-in voltage goes up as the initial gap length increases.

5. Conclusion

In this paper, the RBF collocation method is employed to analyze electroactuated MEMS structures. The accuracy of the method of using the smoothing spline r^n basis and the multiquadric (MQ) basis with different parameters is investigated using several elastostatic examples. Two strategies for distributing collocation points and nodes, namely the uniform distribution and Chebyshev distributions, are adopted in the computation. It is found that both bases and node distribution schemes behave well in the clamped–clamped case. The MQ basis and Chebyshev distribution are superior in the cantilever case but need the consideration of an optimal value for the shape parameter in the MQ basis. In this case, the r^7 basis adopted in analyzing the clamped–clamped beam is preferred although the MQ basis adopted in the cantilevered case gives a higher accuracy.

The results from the RBF collocation method match well with other numerical and experimental results. In fact, only 23 nodes are used in the computation but the RBF method already gives a convergent result in several iterations during the nonlinear solution process. The central difference algorithm and the Newmark algorithm are adopted to calculate the dynamic responses of electroactuated beams. Due to the dependence of the critical time step size in the central difference scheme on the minimum distance of nodes, it is better to employ the Newmark algorithm when the Chebyshev distribution is used.

Finally the influences of beam length, residual stress and initial gap length on the pull-in voltage are investigated. It is demonstrated that increasing the residual stress and initial gap length will increase the pull-in voltage, while increasing the beam length will decrease the pull-in voltage since the bending resistance is lowered.

Acknowledgments

The work described in this paper was supported by a grant from the Research Grants Council of the Hong Kong Special Administration, People's Republic of China (Project No CityU 1185/03E). The first author thanks Professor M-W Lu at the Department of Engineering Mechanics, Tsinghua University, People's Republic of China, for helpful discussions.

References

[1] Senturia S D, Aluru N R and White J 1997 Simulating the behavior of MEMS devices: computational methods and needs *IEEE Comput. Sci. Eng.* **4** 30–43

[2] Legtenberg R, Gilbert J and Senturia S D 1997 Electrostatic curved electrode actuators *J. Microelectromech. Syst.* **6** 257–65

[3] Huang J M *et al* 2001 Mechanical design and optimization of capacitive micromachined switch *Sensors Actuators* A **93** 273–85

[4] Pamidighantam S, Puers R, Baert K and Tilmans H A C 2002 Pull-in voltage analysis of electrostatically actuated beam structures with fixed–fixed and fixed–free end conditions *J. Micromech. Microeng.* **12** 458–64

[5] Bochobza-Degani O and Nemirovsky Y 2002 Modeling the pull-in parameters of electrostatic actuators with a novel lumped two degrees of freedom pull-in model *Sensors Actuators* A **97/98** 569–78

[6] Younis M I, Abdel-Rahman E M and Nayfeh A 2003 A reduced-order model for electrically actuated microbeam-based MEMS *J. Microelectromech. Syst.* **12** 672–80

[7] Cheng J, Zhe J and Wu X 2004 Analytical and finite element model pull-in study of rigid and deformable electrostatic microactuators *J. Micromech. Microeng.* **14** 57–68

[8] Aluru N R and White J 1999 A multilevel Newton method for mixed-energy domain simulation of MEMS *J. Microelectromech. Syst.* **8** 299–308

[9] Collenz A, De Bona F, Gugliotta A and Somà A 2004 Large deflections of microbeams under electrostatic loads *J. Micromech. Microeng.* **14** 365–73

[10] Fedoseyev A I, Friedman M J and Kansa E J 2002 Improved multiquadric method for elliptic partial differential equations via PDE collocation on the boundary *Comput. Math. Appl.* **43** 439–55

[11] Atluri S N and Zhu T 1998 A new meshless local Petrov–Galerkin (MLPG) approach in computational mechanics *Comput. Mech.* **22** 117–27

[12] Zhang X, Liu X H, Song K Z and Lu M W 2001 Least-square collocation meshless method *Int. J. Numer. Methods Eng.* **51** 1089–100

[13] Chen W 2002 Symmetric boundary knot method *Eng. Anal. Bound. Elem.* **26** 489–94

[14] Liu G R and Gu Y T 2001 A point interpolation method for two-dimensional solids *Int. J. Numer. Methods Eng.* **50** 937–51

[15] Wang J G and Liu G R 2002 A point interpolation meshless method based on radial basis functions *Int. J. Numer. Methods Eng.* **54** 1623–48
[16] Liu G R 2002 *Mesh Free Methods: Moving Beyond the Finite Element Method* (Boca Raton, FL: Chemical Rubber Company Press)
[17] Zhang X and Liu Y 2004 *Meshless Methods* (Beijing: Tsinghua University Press) (in Chinese)
[18] Aluru N R 1999 A reproducing kernel particle method for meshless analysis of microelectromechanical systems *Comput. Mech.* **23** 324–38
[19] Li G and Aluru N R 2001 Linear, nonlinear and mixed-regime analysis of electrostatic MEMS *Sensors Actuators* A **91** 278–91
[20] Ohs R R and Aluru N R 2001 Meshless analysis of piezoelectric devices *Comput. Mech.* **27** 23–36
[21] Li G and Aluru N R 2003 Efficient mixed-domain analysis of electrostatic MEMS *IEEE Trans. Comput.-Aided Des. Integr. Circuits Syst.* **22** 1228–42
[22] Zhang X, Song K Z, Lu M W and Liu X 2000 Meshless methods based on collocation with radial basis functions *Comput. Mech.* **26** 333–43
[23] Hon Y C, Lu M W, Xue W M and Zhu Y M 1997 Multiquadric method for the numerical solution of a biphasic mixture model *Appl. Math. Comput.* **88** 153–75
[24] Hon Y C *et al* 2002 Numerical algorithm for triphasic model of charged and hydrated soft tissues *Comput. Mech.* **29** 1–15
[25] Wong S M, Hon Y C and Li T S 2002 A meshless multilayer model for a coastal system by radial basis functions *Comput. Math. Appl.* **43** 585–605
[26] Franke R 1982 Scattered data interpolation: test of some methods *Math. Comput.* **38** 181–200
[27] Wang J G and Liu G R 2002 On the optimal shape parameters of radial basis functions used for 2D meshless methods *Comput. Methods Appl. Mech. Eng.* **191** 2611–30
[28] Ananthasuresh G K, Gupta R K and Senturia S D 1996 An approach to macromodeling of MEMS for nonlinear dynamic simulation *Microelectromechanical Systems (MEMS), ASME Dynamic Systems and Control (DSC) Series* vol 59, pp 401–7
[29] Tilmans H A C and Legtenberg R 1994 Electrostatically driven vacuum-encapsulated polysilicon resonators: Part II. Theory and performance *Sensors Actuators* A **45** 67–84